INTERNATIONAL JOURNAL OF
NUMERICAL ANALYSIS AND MODELING, *SERIES B*
Volume 2, Number 4, Pages 315–337

SIMULATION OF CO_2 PLUME IN POROUS MEDIA: CONSIDERATION OF CAPILLARITY AND BUOYANCY EFFECTS

ARDIANSYAH NEGARA, MOHAMED FATHY EL-AMIN AND SHUYU SUN

Abstract. IMplicit Pressure Explicit Saturation (IMPES) scheme with treating buoyancy and capillary forces is used to solve the two-phase water-CO_2 flow problem. In most of the previous studies of the two-phase flow, the buoyancy force term was ignored; however, in the case of liquid-gas systems such as water-CO_2, the gravity term is very important to express the buoyancy effect. In this paper, we present three numerical examples to study the CO_2 plume in homogeneous, layered, and fractured porous media. In each numerical example, we tested four different models by ignoring both gravity and capillary pressure, considering only gravity, considering only capillary pressure, and considering both gravity and capillary pressure. The cell-centered finite difference (CCFD) method is used to discretize the problem under consideration. Furthermore, we also present the stability analysis of the IMPES scheme. The numerical results demonstrate the effects of the gravity and the capillary pressure on the flow for the four different cases.

Key words. IMPES, stability, carbon dioxide (CO_2) sequestration, two-phase flow, heterogeneous porous media, capillary pressure.

1. Introduction

Carbon dioxide (CO_2) sequestration is one of the most effective methods to reduce the amount of CO_2 in the atmosphere by injecting CO_2 into the geological formations. Furthermore, it has also an important role for the enhanced oil recovery [3, 9, 25, 30, 31]. Numerical investigation of the two-phase flow in porous media with the application on the CO_2 injection has been studied by several authors in the recent years [7, 9, 16, 23, 29, 30]. A coupled system of the time-dependent partial differential equations is used to govern the two-phase flow in porous media. There are several methods to solve these time-dependent partial differential equations such as the fully implicit, IMplicit-EXplicit (IMEX), operator splitting, sequential, and IMplicit Pressure Explicit Saturation (IMPES). The latter is the most well-known method and widely used in the subsurface modeling and simulation. The fully implicit method [6, 15, 26–28] is unconditionally stable; however, it is computationally expensive. The IMEX method [2, 5, 21] is used to solve the ordinary differential equations resulting from the spatial discretization of the time-dependent partial differential equations. The IMEX method is more stable than the fully implicit method because it considers the linear terms implicitly and solves the other terms explicitly. The idea of the operator splitting method [1, 17, 20] is to simplify the original problem into a simpler form by the time-lag dimension. Some authors [20, 22] introduced the iterative operator splitting as a part of the step of iteration in the fully implicit method. The sequential method [33] is a modified version of the IMPES method since the saturation is evaluated implicitly too. Comparing with the fully implicit method, the computational cost of the sequential method is not so expensive in such a way that it is suitable for the large size models where the stability becomes an important consideration.

Received by the editors July 21, 2011 and, in revised form, September 25, 2011.
2000 *Mathematics Subject Classification.* 35R35, 49J40, 60G40.

In the modeling of the two-phase incompressible flow in porous media, the most well-known method that is employed is the IMplicit Pressure Explicit Saturation (IMPES) [11–14, 18, 24, 26, 28]. In this scheme, the pressure equation is evaluated implicitly while the saturation equation is solved explicitly. The pressure equation in the IMPES scheme is obtained after summation of the Darcy's law and substitutes them into the summation of the two mass conservation equations of each phase. After obtaining the pressure, we can calculate the Darcy velocity and the saturation. Since the pressure does not depend on the time, the pressure changes slower than the saturation ones. The implicit part of the pressure calculation takes more time than the explicit part of the saturation computation. Basically, the IMPES method is the fastest scheme based on the per-time step basis. Moreover, the stability condition of the scheme is determined in terms of the given parameters.

From some studies that have been done, from the physical point of view, there is a significant difference between the results considering the capillarity and without the capillarity [4]. The capillary pressures hold up the buoyant flow of the CO_2 plume. Moreover, the capillary pressure together with the relative permeability governs the interactions between the medium and the fluid path. It, however, could be neglected in homogeneous domain but not for heterogeneous one [24]. Therefore, it is important to include the capillarity effects simultaneously with the gravity in this work.

The paper contains several parts: Section 1, in general, is an overview about the motivation and the importance of CO_2 sequestration and its numerical investigation. In section 2, we describe the governing equations for the two-phase flow in porous media for the water-gas system. In section 3, we present the IMPES numerical scheme including both the gravity and the capillary pressure terms which is constructed based on the cell-centered finite difference (CCFD) method, explanation on how to generate the non-uniform mesh, and the treatment of boundary conditions. In section 4, we discuss the stability of the IMPES scheme. Section 5 demonstrates some numerical experiments of the CO_2 injection in the subsurface and the discussion of the results. Finally, we end up with the conclusions in section 6.

2. Mathematical formulations

The basic differential equations that govern the flow of the two-phase incompressible flow in porous media are the saturation equation and the constitutive equation (Darcy's law). Those equations predict the fluid pressure distribution, the velocity, and the phase saturation. In this work, we consider the liquid (water) and the gas (CO_2) fluid phases and we assume there are no effects of the solubility of CO_2 in the water and the salt precipitation. The water phase is indicated by a subscript w and the gas phase is denoted by g. The saturation equation in this paper is defined as follows [23]:

$$\phi \frac{\partial S_\alpha}{\partial t} + \nabla \cdot \mathbf{u}_\alpha = q_\alpha, \ \alpha = w, g, \tag{1}$$

where ϕ is the porosity of the medium, S_α, $\mathbf{u}_\alpha$, and q_α are the saturation, the Darcy velocity, and the source/sink of each phase α, respectively. In the standard notations, $\nabla \cdot (\frac{\partial}{\partial x}, \frac{\partial}{\partial z})^T$ is the partial differential operator where $\nabla = (\frac{\partial}{\partial x}, \frac{\partial}{\partial z})^T$ is the gradient operator and $\nabla\cdot$ is the divergence operator.

The fluid saturations for the two-phase flow of the water and the gas are interrelated by,

$$S_w + S_g = 1 \tag{2}$$

Darcy's law associates the total volumetric flow rate for each fluid phase to the pressure gradient. Besides that, Darcy's law also associates the total volumetric flow rate to the properties of the fluid and the medium such as the viscosity, μ_α, and the effective permeability, k_α. The Darcy velocity of each phase α is defined by,

$$\mathbf{u}_\alpha = -\frac{k_{r\alpha}}{\mu_\alpha}\mathbf{K}(\nabla p_\alpha - \rho_\alpha g \nabla z),\ \alpha = w, g, \tag{3}$$

where $\mathbf{g} = (0, -g)^T$ is the gravitational acceleration.

The flow of the two phase fluids causes to interfere each other by occupying the pore space and resists the other fluid. As a consequence, the fluid with higher saturation is able to flow easier since its cross-section of the flow path in the pores is larger. Therefore, the effective permeability is not greater than absolute permeability in the porous medium [10]. The relative permeability which depends on the gas saturation is given by,

$$k_{r\alpha} = k_{r\alpha}(S_g),\ \alpha = w, g, \tag{4}$$

There are some common formulas to define the relative permeability such as Corey, Naar and Henderson, and van Genuchten (see References [7, 10, 32], respectively). The relative permeability has an important role in the fluid flow behavior. It is obtained by the experiments in the laboratory. The relative permeability has a relationship especially with the history of the wetting phase saturation [19] and the non-wetting phase saturation [23, 32], which is used in this work. The most well-known relative permeability formula for the water-gas system is Brook-Corey [8,23]:

$$k_{rw}(S_g) = (1 - S_{eg})^{\frac{2+3\lambda}{\lambda}} \tag{5}$$

$$k_{rg}(S_g) = S_{eg}^2[1 - (1 - S_{eg})^{\frac{2+\lambda}{\lambda}}] \tag{6}$$

Here, λ is the pore size distribution index. Its value is small (e.g. $\lambda = 0.2$) for heterogeneous material and large (e.g. $\lambda = 3.0$) for homogeneous material [4]. S_{eg}, is the normalized gas phase saturation which is defined by [23]:

$$S_{eg} = \frac{S - S_{rg}}{1 - S_{rg} - S_{rw}} \tag{7}$$

where S_{rg} is the residual saturation of the gas phase and S_{rw} is the residual saturation of the water phase.

The residual saturation is the amount of the phase that is trapped in the pore space. The residual saturation of the non-wetting phase, in this case is the gas (CO_2), is trapped by the capillary forces as,

$$p_c(S_g) = p_g - p_w \tag{8}$$

The capillary forces could make a discontinuity of the pressures between the water and the gas. The capillary forces also cause a discontinuity of the saturation due to the capillarity continuity. The capillary pressure formula that we use in this study refers to Theodoropoulou [32]:

$$p_c = p_c^0\Big(1 - \frac{S_g}{1 - S_{rw}} + b_c\Big)^{-m_c} \tag{9}$$

where p_c is the capillary pressure, p_c^0 is the entry capillary pressure, b_c, and m_c are constants and in this work, their values are equal to 10^{-4} and 3, respectively. Let us define the total velocity as,

$$\mathbf{u}_t = \mathbf{u}_g + \mathbf{u}_w \tag{10}$$

By adding the saturation equations for each phase in (1) and using (2) and (10), we end up with,

$$\nabla \cdot \mathbf{u}_t = q_t, \tag{11}$$

Adding the constitutive equations for each phase in (3) then substitute into (10) by using the correlation in (8), we end up:

$$\mathbf{u}_t = -\mathbf{K}(\lambda_g + \lambda_w)\nabla p_g + \mathbf{K}(\lambda_g \rho_g + \lambda_w \rho_w) g \nabla z + \lambda_w \mathbf{K} \nabla p_c \tag{12}$$

Let's introduce the fractional flow, $f_\alpha = \lambda_\alpha / \lambda_t$, and the mobility, $\lambda_\alpha = k_{r\alpha}/\mu_\alpha$. By rewriting (12), we obtain

$$\mathbf{u}_t = -\mathbf{K}(\lambda_g + \lambda_w)\nabla p_g + \mathbf{K}(f_g \rho_g + f_w \rho_w) \lambda_t g \nabla z + f_w \lambda_t \mathbf{K} \nabla p_c \tag{13}$$

In order to derive the pressure equation, substitute (13) into (11), one may obtain:

$$\nabla \cdot (-\lambda_t \mathbf{K} \nabla p_g + (f_g \rho_g + f_w \rho_w) \lambda_t \mathbf{K} g \nabla z + f_w \lambda_t \mathbf{K} \nabla p_c) = q_t \tag{14}$$

where

$$\lambda_t = \lambda_g + \lambda_w \tag{15}$$

$$q_t = q_g + q_w \tag{16}$$

The saturation can be derived by substituting the constitutive equation for the gas phase in (3) into (1) which will give:

$$\phi \frac{\partial S_g}{\partial t} + \nabla \cdot \mathbf{u}_g = q_g, \tag{17}$$

where the gas velocity

$$\mathbf{u}_g = f_g \mathbf{u}_t - f_g \lambda_w (\rho_w - \rho_g) \mathbf{K} g \nabla z - f_g \lambda_w \mathbf{K} \nabla p_c \tag{18}$$

Note that from the formulation of the pressure and the saturation, the pressure p_g is implicitly evaluated whereas the saturation S_g is explicitly evaluated. This is called as the IMplicit Pressure Explicit Saturation (IMPES) scheme which has been widely exploited for the two-phase flow in the petroleum reservoirs. In the IMPES method, the pressure equation is obtained by substituting the constraint of the saturation and Darcy's law into the mass conservation equation. After obtaining the pressure, the Darcy's law is solved to get the velocity and the saturation.

The primary unknowns from the discussion above are p (pressure) and S (saturation). In this study, the domain is rectangular and bounded with the boundary, $\partial\Omega = \Gamma_D \bigcup \Gamma_N$ where Γ_D is the Dirichlet boundary and Γ_N is the Neumann boundary. The boundary conditions associated to (14) and (17) are:

$$p_w (\text{or } p_g) = p_D \text{ on } x \in \Gamma_D, \tag{19}$$

$$\mathbf{u}_t \cdot \mathbf{n} = q_N \text{ on } x \in \Gamma_N, \tag{20}$$

where $\mathbf{n}$ is the outward unit normal vector on the boundary $\partial\Omega$, p_D is the pressure on Γ_D and q_N is the imposed inflow rate on Γ_N, respectively. The gas phase saturation on the boundary $\partial\Omega$ is

$$S_g (\text{or } S_w) = S_N \text{ on } \Gamma_N. \tag{21}$$

The initial saturation of gas phase on the inlet is defined by

$$S_g = S_g^0 \text{ in } \Omega. \tag{22}$$

3. Numerical scheme

3.1. Discretization and mesh generation. In order to solve the differential system introduced above numerically, we use the cell-centered finite difference (CCFD) method. The CCFD is a finite volume type of method that is very useful and widely used in solving the petroleum reservoir simulation problems. The scheme of cell-centered finite difference is depicted by Figure 1.

In this study, the pressure distribution for each cell along the entire domain is solved by,

(23)
$$\nabla\cdot(-\lambda_t(S_g^n)\mathbf{K}\nabla p_g^{n+1}+(f_g(S_g^n)\rho_g+f_w(S_g^n)\rho_w)\lambda_t(S_g^n)\mathbf{K}g\nabla z+f_w\lambda_t(S_g^n)\mathbf{K}\nabla p_c)=q_t^{n+1}$$

The pressure equation (23) is solved implicitly for p_g and its spatial discretization is defined:

$$\begin{aligned}
&\frac{-\lambda_{t,i,j+\frac{1}{2}}\mathbf{K}_{i,j+\frac{1}{2}}\dfrac{p_{g,i+\frac{1}{2},j+\frac{1}{2}}-p_{g,i-\frac{1}{2},j+\frac{1}{2}}}{x_{i+\frac{1}{2}}-x_{i-\frac{1}{2}}}+\lambda_{t,i+1,j+\frac{1}{2}}\mathbf{K}_{i+1,j+\frac{1}{2}}\dfrac{p_{g,i+\frac{3}{2},j+\frac{1}{2}}-p_{g,i+\frac{1}{2},j+\frac{1}{2}}}{x_{i+\frac{3}{2}}-x_{i+\frac{1}{2}}}}{x_{i+1}-x_i}\\
&+\frac{-\lambda_{t,i+\frac{1}{2},j}\mathbf{K}_{i+\frac{1}{2},j}\dfrac{p_{g,i+\frac{1}{2},j+\frac{1}{2}}-p_{g,i+\frac{1}{2},j-\frac{1}{2}}}{z_{j+\frac{1}{2}}-z_{j-\frac{1}{2}}}+\lambda_{t,i+\frac{1}{2},j+1}\mathbf{K}_{i+\frac{1}{2},j+1}\dfrac{p_{g,i+\frac{1}{2},j+\frac{3}{2}}-p_{g,i+\frac{1}{2},j+\frac{1}{2}}}{z_{j+\frac{3}{2}}-z_{j+\frac{1}{2}}}}{z_{j+1}-z_j}\\
&+\frac{(f_{g,i+\frac{1}{2},j+1}\rho_g+f_{w,i+\frac{1}{2},j+1}\rho_w)\lambda_{t,i+\frac{1}{2},j+1}\mathbf{K}_{i+\frac{1}{2},j+1}g\dfrac{z_{i+\frac{1}{2},j+\frac{3}{2}}-z_{i+\frac{1}{2},j+\frac{1}{2}}}{z_{j+\frac{3}{2}}-z_{j+\frac{1}{2}}}}{z_{j+1}-zj}\\
&-\frac{(f_{g,i+\frac{1}{2},j}\rho_g+f_{w,i+\frac{1}{2},j}\rho_w)\lambda_{t,i+\frac{1}{2},j}\mathbf{K}_{i+\frac{1}{2},j}g\dfrac{z_{i+\frac{1}{2},j+\frac{1}{2}}-z_{i+\frac{1}{2},j-\frac{1}{2}}}{z_{j+\frac{1}{2}}-z_{j-\frac{1}{2}}}}{z_{j+1}-zj}\\
&+\frac{f_{w,i+1,j+\frac{1}{2}}\lambda_{t,i+1,j+\frac{1}{2}}\mathbf{K}_{i+1,j+\frac{1}{2}}\dfrac{p_{c,i+\frac{3}{2},j+\frac{1}{2}}-p_{c,i+\frac{1}{2},j+\frac{1}{2}}}{x_{i+\frac{3}{2}}-x_{i+\frac{1}{2}}}}{x_{i+1}-x_i}\\
&-\frac{f_{w,i,j+\frac{1}{2}}\lambda_{t,i,j+\frac{1}{2}}\mathbf{K}_{i,j+\frac{1}{2}}\dfrac{p_{c,i+\frac{1}{2},j+\frac{1}{2}}-p_{c,i-\frac{1}{2},j+\frac{1}{2}}}{x_{i+\frac{1}{2}}-x_{i-\frac{1}{2}}}}{x_{i+1}-x_i}\\
&+\frac{f_{w,i+\frac{1}{2},j+1}\lambda_{t,i+\frac{1}{2},j+1}\mathbf{K}_{i+\frac{1}{2},j+1}\dfrac{p_{c,i+\frac{1}{2},j+\frac{3}{2}}-p_{c,i+\frac{1}{2},j+\frac{1}{2}}}{z_{j+\frac{3}{2}}-z_{j+\frac{1}{2}}}}{z_{j+1}-z_j}\\
&-\frac{f_{w,i+\frac{1}{2},j}\lambda_{t,i+\frac{1}{2},j}\mathbf{K}_{i+\frac{1}{2},j}\dfrac{p_{c,i+\frac{1}{2},j+\frac{1}{2}}-p_{c,i+\frac{1}{2},j-\frac{1}{2}}}{z_{j+\frac{1}{2}}-z_{j-\frac{1}{2}}}}{z_{j+1}-z_j}\\
&=q_{t,i+\frac{1}{2},j+\frac{1}{2}}^{n+1}
\end{aligned}$$

After obtaining the pressure, the total Darcy velocity (13) is evaluated explicitly:

$$\begin{aligned}\mathbf{u}^x_{t,i,j+\frac{1}{2}} &= -\lambda_{t,i,j+\frac{1}{2}}\mathbf{K}_{i,j+\frac{1}{2}}\frac{p_{g,i+\frac{1}{2},j+\frac{1}{2}}-p_{g,i-\frac{1}{2},j+\frac{1}{2}}}{x_{i+\frac{1}{2}}-x_{i-\frac{1}{2}}}\\ &\quad + f_{w,i,j+\frac{1}{2}}\lambda_{t,i,j+\frac{1}{2}}\mathbf{K}_{i,j+\frac{1}{2}}\frac{p_{c,i+\frac{1}{2},j+\frac{1}{2}}-p_{c,i-\frac{1}{2},j+\frac{1}{2}}}{x_{i+\frac{1}{2}}-x_{i-\frac{1}{2}}}\end{aligned}$$

$$\begin{aligned}\mathbf{u}^x_{t,i+1,j+\frac{1}{2}} &= -\lambda_{t,i+1,j+\frac{1}{2}}\mathbf{K}_{i+1,j+\frac{1}{2}}\frac{p_{g,i+\frac{3}{2},j+\frac{1}{2}}-p_{g,i+\frac{1}{2},j+\frac{1}{2}}}{x_{i+\frac{3}{2}}-x_{i+\frac{1}{2}}}\\ &\quad + f_{w,i+1,j+\frac{1}{2}}\lambda_{t,i+1,j+\frac{1}{2}}\mathbf{K}_{i+1,j+\frac{1}{2}}\frac{p_{c,i+\frac{3}{2},j+\frac{1}{2}}-p_{c,i+\frac{1}{2},j+\frac{1}{2}}}{x_{i+\frac{3}{2}}-x_{i+\frac{1}{2}}}\end{aligned}$$

$$\begin{aligned}\mathbf{u}^z_{t,i+\frac{1}{2},j} &= -\lambda_{t,i+\frac{1}{2},j}\mathbf{K}_{i+\frac{1}{2},j}\frac{p_{g,i+\frac{1}{2},j+\frac{1}{2}}-p_{g,i+\frac{1}{2},j-\frac{1}{2}}}{z_{j+\frac{1}{2}}-z_{j-\frac{1}{2}}}\\ &\quad + (f_{g,i+\frac{1}{2},j}\rho_g + f_{w,i+\frac{1}{2},j}\rho_w)\lambda_{t,i+\frac{1}{2},j}\mathbf{K}_{i+\frac{1}{2},j}g\frac{z_{i+\frac{1}{2},j+\frac{1}{2}}-z_{i+\frac{1}{2},j-\frac{1}{2}}}{z_{j+\frac{1}{2}}-z_{j-\frac{1}{2}}}\\ &\quad + f_{w,i+\frac{1}{2},j}\lambda_{t,i+\frac{1}{2},j}\mathbf{K}_{i+\frac{1}{2},j}\frac{p_{c,i+\frac{1}{2},j+\frac{1}{2}}-p_{c,i+\frac{1}{2},j-\frac{1}{2}}}{z_{j+\frac{1}{2}}-z_{j-\frac{1}{2}}}\end{aligned}$$

$$\begin{aligned}\mathbf{u}^z_{t,i+\frac{1}{2},j+1} &= -\lambda_{t,i+\frac{1}{2},j+1}\mathbf{K}_{i+\frac{1}{2},j+1}\frac{p_{g,i+\frac{1}{2},j+\frac{3}{2}}-p_{g,i+\frac{1}{2},j+\frac{1}{2}}}{z_{j+\frac{3}{2}}-z_{j+\frac{1}{2}}}\\ &\quad + (f_{g,i+\frac{1}{2},j+1}\rho_g + f_{w,i+\frac{1}{2},j+1}\rho_w)\lambda_{t,i+\frac{1}{2},j+1}\mathbf{K}_{i+\frac{1}{2},j+1}g\frac{z_{i+\frac{1}{2},j+\frac{3}{2}}-z_{i+\frac{1}{2},j+\frac{1}{2}}}{z_{j+\frac{3}{2}}-z_{j+\frac{1}{2}}}\\ &\quad + f_{w,i+\frac{1}{2},j+1}\lambda_{t,i+\frac{1}{2},j+1}\mathbf{K}_{i+\frac{1}{2},j+1}\frac{p_{c,i+\frac{1}{2},j+\frac{3}{2}}-p_{c,i+\frac{1}{2},j+\frac{1}{2}}}{z_{j+\frac{3}{2}}-z_{j+\frac{1}{2}}}\end{aligned}$$

Then, by the upwind scheme of the CCFD method, the saturation can be obtained explicitly as follows:

(24)
$$\phi\frac{S_g^{n+1}-S_g^n}{\Delta t^n}+\nabla\cdot(f_g(S_g^n)\mathbf{u}_t^{n+1}) = q_g^{n+1}+\nabla\cdot(f_g(S_g^n)\lambda_w(S_g^n)(\rho_w-\rho_g)\mathbf{K}g\nabla z+f_g\lambda_w(S_g^n)\mathbf{K}\nabla p_c)$$

where Δt^n is the time step length, $\Delta t^n = t^{n+1}-t^n$. To compute the gas saturation, we approximate (24) numerically and particularly for the second term in the left-hand side is solved by the upwind scheme as follows:

$$
\begin{aligned}
&\phi_{i+\frac{1}{2},j+\frac{1}{2}} \frac{(S^{n+1}_{g,i+\frac{1}{2},j+\frac{1}{2}} - S^{n}_{g,i+\frac{1}{2},j+\frac{1}{2}})}{(t^{n+1}-t^{n})} \\
&+\frac{\mathbf{u}^{x(n)}_{t,i+1,j+\frac{1}{2}} f_g(S^{(n)*}_{g,i+1,j+\frac{1}{2}}) - \mathbf{u}^{x(n)}_{t,i,j+\frac{1}{2}} f_g(S^{(n)*}_{g,i,j+\frac{1}{2}})}{x_{i+1}-x_i} \\
&+\frac{\mathbf{u}^{z(n)}_{t,i+\frac{1}{2},j+1} f_g(S^{(n)*}_{g,i+\frac{1}{2},j+1}) - \mathbf{u}^{z(n)}_{t,i+\frac{1}{2},j} f_g(S^{(n)*}_{g,i+\frac{1}{2},j})}{z_{j+1}-z_j} \\
&= q^{n+1}_{g,i+\frac{1}{2},j+\frac{1}{2}} \\
&+f_{g,i+\frac{1}{2},j+1}\lambda_{w,i+\frac{1}{2},j+1}(\rho_w-\rho_g)\mathbf{K}_{i+\frac{1}{2},j+1} g \frac{z_{i+\frac{1}{2},j+\frac{3}{2}} - z_{i+\frac{1}{2},j+\frac{1}{2}}}{z_{j+\frac{3}{2}} - z_{j+\frac{1}{2}}} \\
&-f_{g,i+\frac{1}{2},j}\lambda_{w,i+\frac{1}{2},j}(\rho_w-\rho_g)\mathbf{K}_{i+\frac{1}{2},j} g \frac{z_{i+\frac{1}{2},j+\frac{1}{2}} - z_{i+\frac{1}{2},j-\frac{1}{2}}}{z_{j+\frac{1}{2}} - z_{j-\frac{1}{2}}} \\
&+\frac{f_{g,i+1,j+\frac{1}{2}}\lambda_{w,i+1,j+\frac{1}{2}}\mathbf{K}_{i+1,j+\frac{1}{2}} \frac{p_{c,i+\frac{3}{2},j+\frac{1}{2}} - p_{c,i+\frac{1}{2},j+\frac{1}{2}}}{x_{i+\frac{3}{2}} - x_{i+\frac{1}{2}}}}{x_{i+1}-x_i} \\
&-\frac{f_{g,i,j+\frac{1}{2}}\lambda_{w,i,j+\frac{1}{2}}\mathbf{K}_{i,j+\frac{1}{2}} \frac{p_{c,i+\frac{1}{2},j+\frac{1}{2}} - p_{c,i-\frac{1}{2},j+\frac{1}{2}}}{x_{i+\frac{1}{2}} - x_{i-\frac{1}{2}}}}{x_{i+1}-x_i} \\
&+\frac{f_{g,i+\frac{1}{2},j+1}\lambda_{w,i+\frac{1}{2},j+1}\mathbf{K}_{i+\frac{1}{2},j+1} \frac{p_{c,i+\frac{1}{2},j+\frac{3}{2}} - p_{c,i+\frac{1}{2},j+\frac{1}{2}}}{z_{j+\frac{3}{2}} - z_{j+\frac{1}{2}}}}{z_{j+1}-z_j} \\
&-\frac{f_{g,i+\frac{1}{2},j}\lambda_{w,i+\frac{1}{2},j}\mathbf{K}_{i+\frac{1}{2},j} \frac{p_{c,i+\frac{1}{2},j+\frac{1}{2}} - p_{c,i+\frac{1}{2},j-\frac{1}{2}}}{z_{j+\frac{1}{2}} - z_{j-\frac{1}{2}}}}{z_{j+1}-z_j}
\end{aligned}
$$

where

$$
S^{x(n)*}_{g,i,j+\frac{1}{2}} = \begin{cases}
S^{x(n)*}_{g,i-\frac{1}{2},j+\frac{1}{2}} & \text{if } \mathbf{u}^{x(n)}_{t,i,j+\frac{1}{2}} > 0 \text{ and } i \geq 1, \\
S^{x(n)*}_{g,i+\frac{1}{2},j+\frac{1}{2}} & \text{if } \mathbf{u}^{x(n)}_{t,i,j+\frac{1}{2}} < 0 \text{ and } i \leq M-1, \\
S^{x(n)*}_{g,Bdry,left,j+\frac{1}{2}} & \text{if } \mathbf{u}^{x(n)}_{t,Bdry,left,j+\frac{1}{2}} > 0 \text{ and } i = 1, \\
S^{x(n)*}_{g,Bdry,right,j+\frac{1}{2}} & \text{if } \mathbf{u}^{x(n)}_{t,Bdry,right,j+\frac{1}{2}} < 0 \text{ and } i = M.
\end{cases}
$$

and

$$S^{z(n)*}_{g,i+\frac{1}{2},j} = \begin{cases} S^{z(n)*}_{g,i-\frac{1}{2},j-\frac{1}{2}} & \text{if } \mathbf{u}^{z(n)}_{t,i+\frac{1}{2},j} > 0 \text{ and } j \geq 1, \\ S^{z(n)*}_{g,i+\frac{1}{2},j+\frac{1}{2}} & \text{if } \mathbf{u}^{z(n)}_{t,i+\frac{1}{2},j} < 0 \text{ and } j \leq N-1, \\ S^{z(n)*}_{g,i+\frac{1}{2},Bdry,bottom} & \text{if } \mathbf{u}^{z(n)}_{t,i+\frac{1}{2},Bdry,bottom} > 0 \text{ and } j = 1, \\ S^{z(n)*}_{g,i+\frac{1}{2},Bdry,top} & \text{if } \mathbf{u}^{z(n)}_{t,i+\frac{1}{2},Bdry,top} < 0 \text{ and } j = N. \end{cases}$$

The time step is divided into n time for the total time step [0,T] which is defined as $0 = t^0 < t^1 < ... < t^N = T$. In this study, we discretize the domain into 50×40 non-uniform meshes as shown in Figure 2. The graded meshes around the source injection are finer than the rest of the domain. In other words, the interval of the axis either x or z increases gradually. Let us specify Δx_1 is the width of the first mesh and Δx_M is the width of the last mesh in x-direction, then we can define the ratio:

$$\frac{\Delta x_M}{\Delta x_1} = r \tag{25}$$

The ratio, r, is related with the expansion coefficient of the element size, γ, as follows:

$$r = \gamma^{M-1} \tag{26}$$

To obtain the correlation above, let us consider

$$\Delta x_2 = \gamma \Delta x_1, \Delta x_3 = \gamma \Delta x_2, \Delta x_4 = \gamma \Delta x_3, ..., \Delta x_M = \gamma \Delta x_{M-1} \tag{27}$$

Hence, it can be expressed

$$\Delta x_m = \gamma^{m-1} \Delta x_1 \tag{28}$$

where $m = 1, 2, ..., M$. Consider X_1 is the first endpoint and X_M is the last endpoint. So, the total length of the interval is

$$\begin{aligned} L &= X_M - X_1 \\ &= (1 + \gamma + \gamma^2 + \gamma^3 + ... + \gamma^{M-1}) \Delta x_1 \\ &= \frac{1 - \gamma^M}{1 - \gamma} \Delta x_1 \end{aligned} \tag{29}$$

Similarly, the mesh generation in z-direction is the same as in the x-direction. In summary, the workflow to solve the problems by numerical approaches is presented in the flowchart as shown in Figure 3.

3.2. Treatment of boundary conditions. There are eight types of the boundary condition treatments that are employed in each numerical example as shown by Figure 4. Therefore, there are eight types of the discretization for the pressure, the Darcy velocity, and the saturation equations in area 1 to 8. The following is an example of the discretization of the pressure, the Darcy velocity and the saturation equations in area 1:

- The pressure equation (23):

$$
\begin{aligned}
&\frac{-\lambda_{t,i,j+\frac{1}{2}}\mathbf{K}_{i,j+\frac{1}{2}}\frac{p_{g,i+\frac{1}{2},j+\frac{1}{2}}-p_{g,i-\frac{1}{2},j+\frac{1}{2}}}{x_{i+\frac{1}{2}}-x_{i-\frac{1}{2}}}+\mathbf{u}_{t,Bdry,left}}{\frac{x_{i+1}-x_i}{2}}\\
&+\frac{\mathbf{u}_{t,Bdry,bottom}+\lambda_{t,i+\frac{1}{2},j+1}\mathbf{K}_{i+\frac{1}{2},j+1}\frac{p_{g,i+\frac{1}{2},j+\frac{3}{2}}-p_{g,i+\frac{1}{2},j+\frac{1}{2}}}{z_{j+\frac{3}{2}}-z_{j+\frac{1}{2}}}}{\frac{z_{j+1}-z_j}{2}}\\
&+\frac{(f_{g,i+\frac{1}{2},j+1}\rho_g+f_{w,i+\frac{1}{2},j+1}\rho_w)\lambda_{t,i+\frac{1}{2},j+1}\mathbf{K}_{i+\frac{1}{2},j+1}g\frac{z_{i+\frac{1}{2},j+\frac{3}{2}}-z_{i+\frac{1}{2},j+\frac{1}{2}}}{z_{j+\frac{3}{2}}-z_{j+\frac{1}{2}}}}{\frac{z_{j+1}-z_j}{2}}\\
&-\frac{(f_{g,i+\frac{1}{2},j}\rho_g+f_{w,i+\frac{1}{2},j}\rho_w)\lambda_{t,i+\frac{1}{2},j}\mathbf{K}_{i+\frac{1}{2},j}g\frac{z_{i+\frac{1}{2},j+\frac{1}{2}}-z_{Bdry,bottom}}{z_{j+\frac{1}{2}}-z_{Bdry,bottom}}}{\frac{z_{j+1}-z_j}{2}}\\
&+\frac{f_{w,i+1,j+\frac{1}{2}}\lambda_{t,i+1,j+\frac{1}{2}}\mathbf{K}_{i+1,j+\frac{1}{2}}\frac{p_{c,i+\frac{3}{2},j+\frac{1}{2}}-p_{c,i+\frac{1}{2},j+\frac{1}{2}}}{x_{i+\frac{3}{2}}-x_{i+\frac{1}{2}}}}{x_{i+1}-x_i}\\
&+\frac{f_{w,i+\frac{1}{2},j+1}\lambda_{t,i+\frac{1}{2},j+1}\mathbf{K}_{i+\frac{1}{2},j+1}\frac{p_{c,i+\frac{1}{2},j+\frac{3}{2}}-p_{c,i+\frac{1}{2},j+\frac{1}{2}}}{z_{j+\frac{3}{2}}-z_{j+\frac{1}{2}}}}{z_{j+1}-z_j}\\
&=q^{n+1}_{t,i+\frac{1}{2},j+\frac{1}{2}}
\end{aligned}
$$

- The Darcy velocity (13):

$$\mathbf{u}^x_{t,i,j+\frac{1}{2}}=\mathbf{u}_{t,Bdry,left}$$

$$
\begin{aligned}
\mathbf{u}^x_{t,i+1,j+\frac{1}{2}} &= -\lambda_{t,i+1,j+\frac{1}{2}}\mathbf{K}_{i+1,j+\frac{1}{2}}\frac{p_{g,i+\frac{3}{2},j+\frac{1}{2}}-p_{g,i+\frac{1}{2},j+\frac{1}{2}}}{x_{i+\frac{3}{2}}-x_{i+\frac{1}{2}}}\\
&\quad+f_{w,i+1,j+\frac{1}{2}}\lambda_{t,i+1,j+\frac{1}{2}}\mathbf{K}_{i+1,j+\frac{1}{2}}\frac{p_{c,i+\frac{3}{2},j+\frac{1}{2}}-p_{c,i+\frac{1}{2},j+\frac{1}{2}}}{x_{i+\frac{3}{2}}-x_{i+\frac{1}{2}}}
\end{aligned}
$$

$$\mathbf{u}^z_{t,i+\frac{1}{2},j}=0$$

$$
\begin{aligned}
&\mathbf{u}^z_{t,i+\frac{1}{2},j+1}\\
= \;& -\lambda_{t,i+\frac{1}{2},j+1}\mathbf{K}_{i+\frac{1}{2},j+1}\frac{p_{g,i+\frac{1}{2},j+\frac{3}{2}}-p_{g,i+\frac{1}{2},j+\frac{1}{2}}}{z_{j+\frac{3}{2}}-z_{j+\frac{1}{2}}}\\
&+(f_{g,i+\frac{1}{2},j+1}\rho_g+f_{w,i+\frac{1}{2},j+1}\rho_w)\lambda_{t,i+\frac{1}{2},j+1}\mathbf{K}_{i+\frac{1}{2},j+1}g\frac{z_{i+\frac{1}{2},j+\frac{3}{2}}-z_{i+\frac{1}{2},j+\frac{1}{2}}}{z_{j+\frac{3}{2}}-z_{j+\frac{1}{2}}}\\
&+f_{w,i+\frac{1}{2},j+1}\lambda_{t,i+\frac{1}{2},j+1}\mathbf{K}_{i+\frac{1}{2},j+1}\frac{p_{c,i+\frac{1}{2},j+\frac{3}{2}}-p_{c,i+\frac{1}{2},j+\frac{1}{2}}}{z_{j+\frac{3}{2}}-z_{j+\frac{1}{2}}}
\end{aligned}
$$

- The saturation equation (24):

$$
\begin{aligned}
&\phi_{i+\frac{1}{2},j+\frac{1}{2}} \frac{(S^{n+1}_{g,i+\frac{1}{2},j+\frac{1}{2}} - S^{n}_{g,i+\frac{1}{2},j+\frac{1}{2}})}{(t^{n+1}-t^{n})} \\
&+ \frac{\mathbf{u}^{x(n)}_{t,i+1,j+\frac{1}{2}} f_g(S^{(n)*}_{g,i+1,j+\frac{1}{2}}) - \mathbf{u}^{x(n)}_{t,Bdry,left} f_g(S^{(n)*}_{g,Bdry,left})}{\frac{x_{i+1}-x_i}{2}} \\
&+ \frac{\mathbf{u}^{z(n)}_{t,i+\frac{1}{2},j+1} f_g(S^{(n)*}_{g,i+\frac{1}{2},j+1}) - \mathbf{u}^{z(n)}_{t,Bdry,bottom} f_g(S^{(n)*}_{g,Bdry,bottom})}{\frac{z_{j+1}-z_j}{2}} \\
&= q^{n+1}_{g,i+\frac{1}{2},j+\frac{1}{2}} \\
&+ f_{g,i+\frac{1}{2},j+1} \lambda_{w,i+\frac{1}{2},j+1} (\rho_w - \rho_g) \mathbf{K}_{i+\frac{1}{2},j+1} g \frac{z_{i+\frac{1}{2},j+\frac{3}{2}} - z_{i+\frac{1}{2},j+\frac{1}{2}}}{z_{j+\frac{3}{2}} - z_{j+\frac{1}{2}}} \\
&- f_{g,i+\frac{1}{2},j} \lambda_{w,i+\frac{1}{2},j} (\rho_w - \rho_g) \mathbf{K}_{i+\frac{1}{2},j} g \frac{z_{i+\frac{1}{2},j+\frac{1}{2}} - z_{Bdry,bottom}}{z_{j+\frac{1}{2}} - z_{Bdry,bottom}} \\
&+ \frac{f_{g,i+1,j+\frac{1}{2}} \lambda_{w,i+1,j+\frac{1}{2}} \mathbf{K}_{i+1,j+\frac{1}{2}} \frac{p_{c,i+\frac{3}{2},j+\frac{1}{2}} - p_{c,i+\frac{1}{2},j+\frac{1}{2}}}{x_{i+\frac{3}{2}} - x_{i+\frac{1}{2}}}}{x_{i+1} - x_i} \\
&+ \frac{f_{g,i+\frac{1}{2},j+1} \lambda_{w,i+\frac{1}{2},j+1} \mathbf{K}_{i+\frac{1}{2},j+1} \frac{p_{c,i+\frac{1}{2},j+\frac{3}{2}} - p_{c,i+\frac{1}{2},j+\frac{1}{2}}}{z_{j+\frac{3}{2}} - z_{j+\frac{1}{2}}}}{z_{j+1} - z_j}
\end{aligned}
$$

Principally, the other boundary condition treatments such as area 2 to 8 are similar. It is important to consider carefully during the discretization for the treatment of the cell that is located outside of the domain. We can consider it in the boundary of the domain or take it as the closest cell to the boundary. The treatment depends on the types of the boundary condition. For instance, in the discretization of area 1 (inlet) above, the term in the first derivative of the gas pressure along x-direction is substituted by the Neumann boundary that is defined as the velocity. Another slightly different treatment of the boundary condition is in the term of the first derivative of the capillary pressure, either in the pressure or the saturation equations. Since the capillary pressure is considered in the center of the cell, there is no capillary pressure defined in the edge of the cell, particularly in the boundary. In this case, we consider that the capillary pressure in the boundary is taken as the same as the one that is located in the closest cell to the boundary. Therefore, the second term of the capillary pressure in x and z-directions are vanished.

4. Stability analysis of the IMPES scheme

The stability issue in the IMPES method is very important because the computational cost required by this method is expensive since this scheme needs very small time step. In this section, we discuss the stability condition of the finite difference scheme. The finite difference scheme is classified to be stable if the error at n^{th} time step does not propagate to the $(n+1)^{th}$ time step. As what has been discussed earlier, there are two main equations to be solved implicitly and explicitly, i.e., the pressure and the saturation equations, respectively. The saturation equation is the

only equation that depends on the time. The pressure, however, does not change rapidly in time compared to the saturation. Therefore, the time steps affect only on the explicit calculation of the saturation.

Let's introduce Φ which is defined as $\Phi_\alpha = p_\alpha + \rho_\alpha g z$. Reformulating the total velocity (10) based on Φ definition, we obtain:

$$\mathbf{u}_t = -\lambda_t \mathbf{K}\nabla\Phi_g + \lambda_w \mathbf{K}\nabla\Phi_c \tag{30}$$

where

$$\Phi_c = \Phi_g - \Phi_w \tag{31}$$

Substituting the newly defined total velocity above to the mass conservation equation (11), the pressure equation becomes:

$$\nabla\cdot(-\lambda_t(S_g^n)\mathbf{K}\nabla\Phi_g^{n+1} + \lambda_w(S_g^n)\mathbf{K}\nabla\Phi_c^n) = q_t^{n+1} \tag{32}$$

Using the CCFD method and applying it to the pressure equation (32),

$$\mathbf{A}_p(\mathbf{S}_g^n)\Phi_g^{n+1} + \mathbf{A}_c(\mathbf{S}_g^n)\Phi_c^n = \mathbf{Q}_t^{n+1} \tag{33}$$

Likewise, using the Φ definition above for the gas phase into the gas velocity, the saturation equation (17) is written as

$$\phi\frac{S_g^{n+1} - S_g^n}{\Delta t} - \nabla\cdot(\lambda_g(S_g^n\mathbf{K}\nabla\Phi_g^{n+1}) = q_g^{n+1} \tag{34}$$

and after applying the CCFD method

$$\mathbf{P}\frac{\mathbf{S}_g^{n+1} - \mathbf{S}_g^n}{\Delta t} + \mathbf{A}_g(\mathbf{S}_g^n)\Phi_g^{n+1} = \mathbf{Q}_g^{n+1} \tag{35}$$

From the equations above, either in pressure or saturation equations, it is clearly shown that $\mathbf{A}_p$, $\mathbf{A}_c$, and $\mathbf{A}_g$ depend on $\mathbf{S}_g$. $\mathbf{P}$ is a diagonal matrix that replaces the porosity in the saturation equation. For the stability analysis that is discussed in the following, the effect of the error saturation on the matrices $\mathbf{A}_p$, $\mathbf{A}_c$, and $\mathbf{A}_g$ is ignored. Rewrite (33) in terms of Φ_g^{n+1} as

$$\Phi_g^{n+1} = \mathbf{A}_p^{-1}(\mathbf{S}_g^n)(\mathbf{Q}_t^{n+1} - \mathbf{A}_c(\mathbf{S}_g^n)\Phi_c(\mathbf{S}_g^n)) \tag{36}$$

Substituting (36) into (35), it follows that

$$\mathbf{S}_g^{n+1} = \mathbf{S}_g^n + \Delta t\mathbf{P}^{-1}\mathbf{Q}_g^{n+1} - \Delta t\mathbf{P}^{-1}\mathbf{A}_g(\mathbf{S}_g^n)\mathbf{A}_p^{-1}(\mathbf{S}_g^n)(\mathbf{Q}_t^{n+1} - \mathbf{A}_c\Phi_c(\mathbf{S}_g^n)) \tag{37}$$

Define the perturbed saturation at n^{th} and $(n+1)^{th}$ time step by

$$\widetilde{\mathbf{S}}_g^n = \mathbf{S}_g^n + \delta\mathbf{S}_g^n \tag{38}$$

and

$$\widetilde{\mathbf{S}}_g^{n+1} = \mathbf{S}_g^{n+1} + \delta\mathbf{S}_g^n \tag{39}$$

Note that $\delta\mathbf{S}_g^n$ and $\delta\mathbf{S}_g^{n+1}$ are the error for $\mathbf{S}_g^n$ and $\mathbf{S}_g^{n+1}$, respectively. In accordance with $\mathbf{S}_g^{n+1}$, $\widetilde{\mathbf{S}}_g^{n+1}$ is given by

$$\widetilde{\mathbf{S}}_g^{n+1} = \widetilde{\mathbf{S}}_g^n + \Delta t\mathbf{P}^{-1}\mathbf{Q}_g^{n+1} - \Delta t\mathbf{P}^{-1}\mathbf{A}_g(\mathbf{S}_g^n)\mathbf{A}_p^{-1}(\mathbf{S}_g^n)\left[\mathbf{Q}_t^{n+1} - \mathbf{A}_c(\mathbf{S}_g^n)\Phi_c(\widetilde{\mathbf{S}}_g^n)\right] \tag{40}$$

Subtracting (37) from (40), it follows that

$$\begin{aligned}\delta\mathbf{S}_g^{n+1} &= \delta\mathbf{S}_g^n + \Delta t\mathbf{P}^{-1}\mathbf{A}_g(\mathbf{S}_g^n)\mathbf{A}_p^{-1}(\mathbf{S}_g^n)\mathbf{A}_c(\mathbf{S}_g^n)\left[\Phi_c(\widetilde{\mathbf{S}}_g^n) - \Phi_c(\mathbf{S}_g^n)\right] \\ &\approx \delta\mathbf{S}_g^n + \Delta t\mathbf{P}^{-1}\mathbf{A}_g(\mathbf{S}_g^n)\mathbf{A}_p^{-1}(\mathbf{S}_g^n)\mathbf{A}_c(\mathbf{S}_g^n)\Phi_c^{'}(\mathbf{S}_g^n)\delta\mathbf{S}_g^n \end{aligned} \tag{41}$$

where

$$\Phi_c^{'}(\mathbf{S}_g^n) = \begin{pmatrix} \Phi_c^{'}(\mathbf{S}_{g_1}^n) \\ \Phi_c^{'}(\mathbf{S}_{g_2}^n) \\ \vdots \\ \vdots \\ \vdots \\ \Phi_c^{'}(\mathbf{S}_{g_{M\times N}}^n) \end{pmatrix}$$

The number of the elements of the vector $\Phi_c^{'}(\mathbf{S}_g^n)$ is equal with the total number of the meshes. Following this stability analysis, therefore, the scheme is said stable if it satisfies the following condition

$$\rho(\mathbf{I} + \Delta t \mathbf{P}^{-1}\mathbf{A}_g(\mathbf{S}_g^n)\mathbf{A}_c(\mathbf{S}_g^n)\Phi_c^{'}(\mathbf{S}_g^n)) < 1 \tag{42}$$

where $\rho(\cdot)$ is the spectral radius and $\mathbf{I}$ is the identity matrix. In the problem under consideration, Δt is taken in the range of 3000-3600 seconds in order to achieve the stability condition.

5. Numerical results

In this section, we present three numerical examples of the CO_2 plume in homogeneous, heterogeneous (layered), and fractured porous media. We simulate four different cases by ignoring the gravity and the capillarity, considering only the gravity, considering only the capillarity, and considering both the gravity and the capillarity. The two-dimensional domain size is 150m $\times$ 120m, in x and z axes, respectively. We assume that the domain is in the deep geological formations. The domain is discretized into 2000 non-uniform mesh elements using the above mesh generation way. The porosity of the medium is taken as 20%. The rock is initially fully saturated with water and CO_2 is injected at the bottom-left corner with a constant flow rate of 0.1 pore volume injection (PVI)/year. On the right boundary, we impose a constant pressure of 5 atm. The top and the bottom of the domain are impermeable layers. For the fluid properties parameters such as the densities, the viscosities, the residual saturations, and the relative permeabilities, we refer to Hayek et al. [23] as presented in Table 1.

5.1. Homogeneous porous medium. In the first example, we consider a two-phase incompressible flow in a two-dimensional homogeneous domain. The permeability of the entire medium is taken as 1 md. From Figures 5a and 5c, it can be seen that the CO_2 saturation distributions of the case without considering the gravity and the capillary pressure and the case due to the capillary pressure only after one year of the injection are quite similar. Their saturation rates, however, are different. The CO_2 saturation distribution without the combination of the gravity and the capillarity has a higher maximum CO_2 saturation, around 0.8, compared with the CO_2 saturation distribution that is affected only by the capillary pressure. Moreover, if we compare it with the CO_2 saturation distribution for the case of combination of the gravity and the capillary pressure (Figure 5d), the result still lower than without considering gravity and capillary pressure. Figure 5b shows the CO_2 saturation distribution by considering only the gravity effect. As expected, from this figure, it seems that the CO_2 rises buoyantly from the source injection since the density of CO_2 is less dense than the density of water. From the results, we can note some effects of the gravity and the capillarity. One of the effects is the capillary pressure retards the distribution of CO_2 in such a way that the cases that

TABLE 1. Parameters for the three examples.

Parameter	Example 1	Example 2	Example 3
Domain dimensions	150m × 120m	150m × 120m	150m × 120m
Rectangular non-uniform mesh	50 × 40	50 × 40	50 × 40
The properties of the porous media:			
ϕ	20%	20%	20%
$\mathbf{K}$(md)	1 md	100 md, 50 md, 20 md, 1 md	1 md, 300 md
The fluid properties:			
μ_g(kg m$^{-1}s^{-1}$)	5.916×10^{-5}	5.916×10^{-5}	5.916×10^{-5}
μ_w(kg m$^{-1}s^{-1}$)	6.922×10^{-4}	6.922×10^{-4}	6.922×10^{-4}
ρ_g(kg m^{-3})	716.7	716.7	716.7
ρ_w(kg m^{-3})	997.42	997.42	997.42
S_{rg}	0.001	0.001	0.001
S_{rw}	0.2	0.2	0.2
k_{rg}	Brooks-Corey	Brooks-Corey	Brooks-Corey
k_{rw}	Brooks-Corey	Brooks-Corey	Brooks-Corey
Initial saturation:			
S^0	0.001	0.001	0.001
Boundary conditions:			
Inlet: injection rate (PVI/year)	0.1	0.1	0.1
Outlet: constant pressure (atm)	5	5	5
p_c^0 (Pa)	10000	10000	10000
Constant parameter:			
λ	2	2	2
m_c	3	3	3

include the capillarity effect have a lower CO_2 saturation rate compared to the one without considering the gravity and the capillarity.

Figures 6a-c display the CO_2 saturation distributions with respect to the depth at 3.7m, 8.9m, and 34.2 m. From these figures, we can clearly see not only the CO_2 saturation distribution for the case of ignoring the gravity and the capillarity but also for the case that considers the capillary pressure which have higher rate of CO_2 saturation compared with the other two cases. Particularly for the cases that include the gravity force effect, we can see that the curves reaching the maximum saturation rate at a certain depth. This means the gravity force contributes to the CO_2 saturation distribution.

5.2. Layered porous medium. In the second example, we consider the two-phase incompressible flow in the two-dimensional heterogeneous domain that consists of four layers as shown by Figure 7. Similarly, we consider the four cases, ignoring the gravity and the capillarity, considering only the gravity effect, considering only the capillarity, and combining both the gravity and the capillarity. The permeabilities of the medium are 100 md, 50 md, 10 md, and 1 md.

Figures 8a-d show the CO_2 saturation distributions after one year of the injection in the heterogeneous domain consist of four layers for four different considered cases. The permeability of the layers is decreasing with respect to the depth from the point source injection. The CO_2 saturation distribution for the case of ignoring both the gravity and the capillary pressure is shown by Figure 8a. From this figure, we can see that the CO_2 saturation distribution seems slue due to the transition from the high permeability, i.e., 100 md to the lower permeability, i.e., 50 md. Figure 8b illustrates the CO_2 saturation distribution by the gravity force effect. Again, as expected, the CO_2 migrates to the top of the reservoir due to the density difference

between CO_2 and water. The force causing the upward migration is called buoyancy force. It is expected that the injected CO_2 will be accumulated on the top of the reservoir after a long time of injection. Figure 8c illustrates the CO_2 saturation distribution for the case that considers only the capillary pressure. If we compare it with the CO_2 saturation distribution for the case of ignoring both the gravity and the capillary pressure, we are obviously able to see the influence of the capillary pressure. The capillary pressure contributes the injected CO_2 to spread more widely in the medium. The case of considering gravity and capillary pressure is displayed by Figure 8d. The capillary pressure drives the injected CO_2 to flow in some areas in the domain in such a way that there is a slightly different distribution with the result of the case that considers only the gravity force.

Figures 9a-c show the CO_2 saturation distributions with respect to the depth at 3.7m, 8.9m, and 34.2 m. It is clearly visible that the CO_2 saturation distribution for the case of ignoring both the gravity and the capillarity always has the highest CO_2 saturation rate at the deepest depth, i.e., 120m. This is because there is no gravity that drives the CO_2 saturation spread upward quickly. Furthermore, the case that considers only the capillary pressure displays the high CO_2 saturation around the injection area. From the numerical results, it is shown clearly that the two cases that are involving the gravity effect have a typical curve. The small difference of the CO_2 saturation between them is distinguished by the presence of the capillary pressure. In conclusion, there are three aspects that affect the CO_2 saturation distribution along the entire domain which cover the permeability distributions, the gravity and the capillary pressure.

5.3. Fractured porous medium. In the third example, we present a two-phase incompressible flow in a two-dimensional fractured domain. Fracture is defined as the separation of a material (rock) into two or more pieces due to an applied stress working on it. Since the rock is separated into some pieces, it allows a fluid to flow rapidly. The fractures are usually connected to the other fractures in such a way that they build networks (depicted by the red lines) as shown in Figure 10. Similar to the two previous cases, we consider the four mentioned cases by considering and ignoring the effects of the gravity and the capillarity. The permeability of medium is 300 md for the fractures and 1 md for the rest of the domain.

Figure 11a shows the CO_2 saturation distribution for the case of ignoring the gravity and the capillarity after one year of injection. From this figure, as expected, the injected CO_2 tends to flow through the fractures than the matrix because of their high permeability. The CO_2 saturation distribution with the gravity effect is shown in Figure 11b. There is a slight difference for the numerical results particularly around the injection area where the injected CO_2 seems to rise buoyantly. The injected CO_2 is also seen to migrate upward more around the deepest fracture compared to the case of ignoring the gravity and the capillary pressure. Figure 11c displays the CO_2 saturation distribution for the case of considering only the capillary pressure. The result indicates the CO_2 spreads more widely around the fractures. The injected CO_2 occupies all of the fractures. If we compare those three numerical results (Figures 11a-c) with the case by considering both the gravity and the capillarity effects (Figure 11d), it is seen that the CO_2 saturation rate of this case in the fractures is the highest.

Figures 12a-c depict the CO_2 saturation distributions with respect to the depth at 3.7m, 8.9m, and 34.2 m. From these figures, we see some up and down curves. This is due to the fracture networks. The CO_2 saturation rate becomes higher once the injected CO_2 occupies the fractures. The CO_2 saturation rate around the

source for the case of ignoring the gravity and the capillarity is high, similar to the homogeneous and the layered porous media cases. One interesting case from the results that needs more attention is the behavior of the CO_2 saturation rate at a certain point, in this case at $x = 34.2$ m (Figure 12c). At this point, it can be seen that the two cases which are ignoring the capillary pressure have higher rate of CO_2 saturation at the fractures than the other two cases which are considering the capillary pressure. Conversely, the two cases with the capillary pressure effect have higher rate of CO_2 saturation in the area outside of the fractures compared with the other two cases which are neglecting the capillary pressure. In other words, the capillary pressure retards the injected CO_2 to flow in the fractures.

6. Conclusions

We have studied the CO_2 injection for homogeneous, layered, and fractured porous media numerically by the IMPES scheme. The numerical results demonstrate the influences of the gravity and the capillary pressure on the modeling of the two-phase CO_2-water system. The gravity force leads the injected CO_2 to rise buoyantly due to the density difference between CO_2 and water. Meanwhile, the capillary pressure compensates the upward migration of the CO_2 saturation distribution to the horizontal direction. In other words, the capillary pressure retards the buoyancy force. Therefore, the rate of the CO_2 saturation distribution for the case that involves both the gravity and the capillary pressure is lower compared with the other three cases. Theoretically, the conclusions in this study show similarities with the results that have been done by Altundas [4].

References

[1] E. Abreu, J. Douglas, F. Furtado and F. Pereira, Operator splitting for three-phase flow in heterogeneous porous media, Community of Computational Physics, 6(1) (2009) 72-84.

[2] G. Akrivis, M. Crouzeix, and C. Makridakis, Implicit-explicit multistep methods for quasilinear parabolic equations, Numerical Mathematic, 82(4) (1999) 521-41.

[3] S. A. Alavian and C. H. Whitson, Modeling of CO_2 injection in a fractured chalk experiment, SPE 125362, presented at the SPE/EAGE Reservoir Characterization and Simulation Conference, 19-21 October 2009, Abu Dhabi, UAE.

[4] Y. B. Altundas, T. S. Ramakrishnan, N. Chugunov, and R. deLoubens, Retardation of CO_2 due to capillary pressure hysteresis: a new CO_2 trapping mechanism, SPE 139641, presented at the SPE International Conference on CO_2 Capture, Storage, and Utilization, 10-12 November 2010, New Orleans, Louisiana, USA.

[5] U. Ascher, S. J. Ruuth, and B. T. R. Wetton, Implicit-explicit methods for time-dependent partial differential equations, SIAM Journal of Numerical Analysis, 32(3) (1995) 797-823.

[6] K. Aziz and A. Settari, Petroleum Reservoir Simulation, Applied Science Publication, London, 1979.

[7] A. Bielinski, Numerical Simulation of CO_2 Sequestration in Geological Formations, Ph.D Thesis, University of Stuttgart, 2007.

[8] R. H. Brooks and A. T. Corey, Hydraulic properties of porous media, Hydrology Papers, Colorado State University, 1964.

[9] J. F. Cameiro, Numerical simulations on the influence of matrix diffusion to carbon sequestration in double porosity fissured aquifers, International Journal of Greenhouse Gas Control, 3(4) (2009) 431-43.

[10] Z. Chen, Reservoir Simulation: Mathematical Techniques in Oil Recovery, CBMS-NSF, Regional Conferences Series in Applied Mathematics, SIAM, Philadelphia, 2007.

[11] Z. Chen, G. Huan, and B. Li, An improved IMPES method for two-phase flow in porous media, Transport in Porous Media, 54(3) (2004) 361-76.

[12] Z. Chen, G. Huan, and Y. Ma, Computational Methods for Multiphase Flows in Porous Media, SIAM Computational Science and Engineering, 2006.

[13] K. H. Coats, A note on IMPES and some IMPES-based simulation models, SPE 49774, presented at the SPE Reservoir Simulation Symposium, 14-17 February 1999, Houston, Texas.

[14] K. H. Coats, IMPES stability: the CFL limit, SPE 85956, SPE Journal 8(3) (2003) 291-97.
[15] D. A. Collins, L. X. Nghiem, Y. K. Li, and J. E. Grabenstetter, An efficient approach to adaptive implicit compositional simulation with an equation of state, SPE 15133, SPE Reservoir Engineering, 7(2) (1992) 259-64.
[16] C. Doughty, Modeling geologic storage of carbon dioxide: comparison of non-hysteretic and hysteretic characteristics curves, Energy Conversion and Management, 48(6) (2007) 1768-81.
[17] J. Douglas, D. W. Peaceman, and H. H. Rachford, A method for calculating multi-dimensional immiscible displacement, Transactions, AIME, 216 (1959) 297-308.
[18] R. G. Fagin and C. H. Stewart Jr., A new approach to the two-dimensional multiphase reservoir simulator, SPE 1188, SPE Journal, 6(2) (1966) 175-82.
[19] J. R. Fanchi, Principles of Applied Reservoir Simulation, Gulf Professional Publishing, Burlington, 2006.
[20] I. Farago, A modified iterated operator splitting method, Applied Mathematical Modelling, 32(8) (2008) 1542-51.
[21] J. Frank, W. Hundsdorfer, and J. G. Verwer, On the stability of implicit-explicit linear multistep methods, Applied Numerical Mathematics, 25(2-3) (1997) 193-205.
[22] J. Geiser, Iterative operator-splitting methods with higher-order time integration methods and applications for parabolic partial differential equations, Journal of Computational and Applied Mathematics, 217(1) (2008), 227-42.
[23] M. Hayek, E. Mouche, and C. Mugler, Modeling vertical stratification of CO_2 injected into a deep layered aquifer, Advances in Water Resources, 32(3) (2009) 450-62.
[24] H. Hoteit and A. Firoozabadi, Numerical modeling of two-phase flow in heterogeneous permeable media with different capillary pressures, Advances in Water Resources, 31(1) (2008), 56-73.
[25] K. Jessen, A. R. Kovscek, and F. M. Orr Jr., Increasing CO_2 storage in oil recovery, Energy Conversion and Management, 46(2) (2005) 293-311.
[26] J. Kou and S. Sun, A new treatment of capillarity to improve the stability of IMPES two-phase flow formulation, Computer and Fluids, 39(10) (2010) 1923-31.
[27] J. Kou and S. Sun, On iterative IMPES formulation for two-phase flow with capillarity in heterogeneous porous media, International Journal of Numerical Analysis and Modeling, Series B, 1(1) (2010) 20-40.
[28] J. E. P. Monteagudo and A. Firoozabadi, Comparison of fully implicit and IMPES formulations for simulation of water injection in fractured and unfractured media, International Journal of Numerical Method in Engineering, 69(4) (2007) 698-728.
[29] K. Sasaki, T. Fujii, Y. Niibori, T. Ito, and T. Hashida, Numerical simulation of supercritical CO_2 injection into subsurface rock masses, Energy Conversion and Management, 49(1) (2008) 54-61.
[30] M. A. Sbai and M. Azaroual, Numerical modeling of formation damage by two-phase particulate transport processes during CO_2 injection in deep heterogeneous porous media, Advances in Water Resources, 34(1) (2011) 62-82.
[31] A. Ravagnani, E. L. Ligero and, S. B. Suslick, CO_2 sequestration through enhanced oil recovery in a mature oil field, Journal of Petroleum Science and Engineering, 65(3-4) (2009) 129-38.
[32] M. A. Theodoropoulou, V. Sygouni, V. Karoutsos, and C. D. Tsakiroglou, Relative permeability and capillary pressure functions of porous media as related to the displacement growth pattern, International Journal of Multiphase Flow, 31(10-11) (2005) 1155-80.
[33] J. Watts, A compositional formulation of the pressure and the saturation equations, SPE 12244, SPE Reservoir Engineering, 1(3) (1986) 243-52.

Computational Transport Phenomena Laboratory, Division of Physical Science and Engineering, King Abdullah University of Science and Technology, Thuwal 23955-6900, Kingdom of Saudi Arabia

E-mail: shuyu.sun@kaust.edu.sa

URL: http://web.kaust.edu.sa/faculty/ShuyuSun/

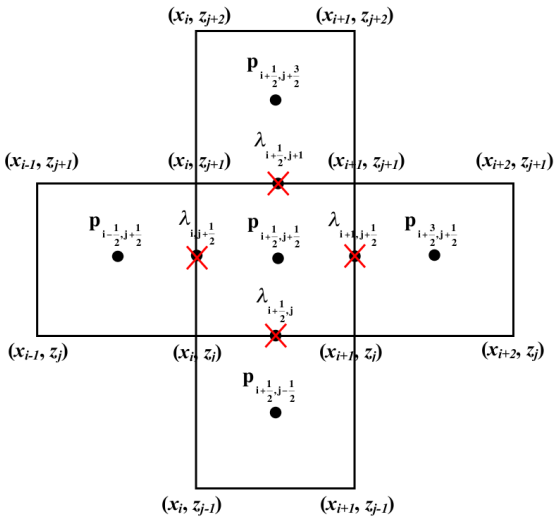

FIGURE 1. A cell-centered finite difference.

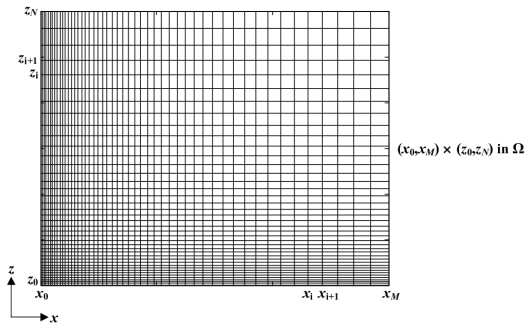

FIGURE 2. The discretization of the domain into 50 × 40 non-uniform mesh.

x-direction: $x_0 < x_1 < ... < x_i < x_{i+1} < ...x_M; i = 1, 2, ...M$

z-direction: $z_0 < z_1 < ... < z_j < z_{j+1} < ...z_N; j = 1, 2, ...N$

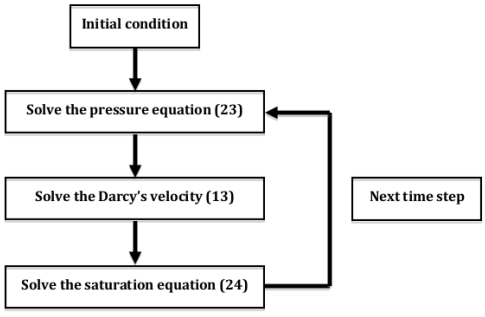

FIGURE 3. The flowchart of the programming design to execute the problem examples.

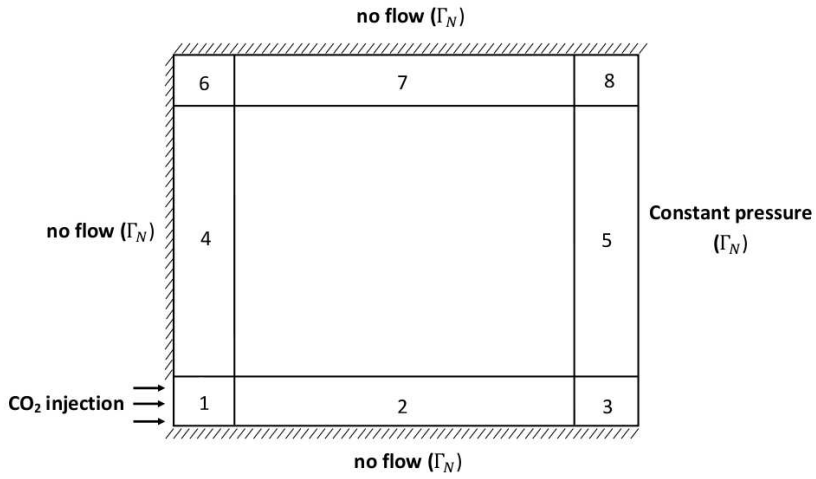

FIGURE 4. Eight types of the boundary condition treatments of the domain.

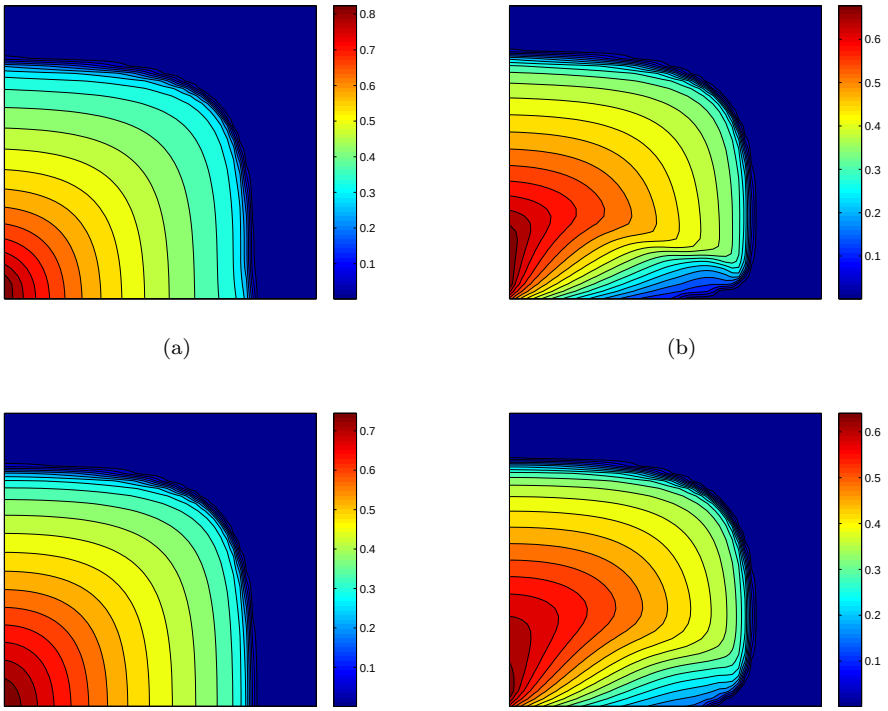

FIGURE 5. CO_2 saturation profiles in the homogeneous domain after one year of injection for four different cases: (a) without the gravity and the capillarity, (b) the gravity effect only, (c) the capillarity effect only, and (d) with the gravity and the capillarity.

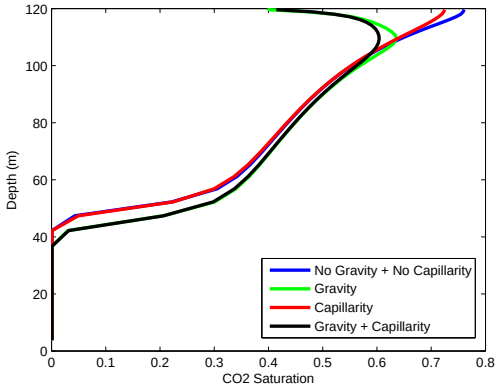

(a)

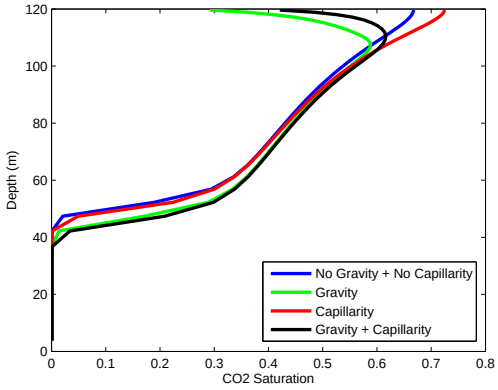

(b)

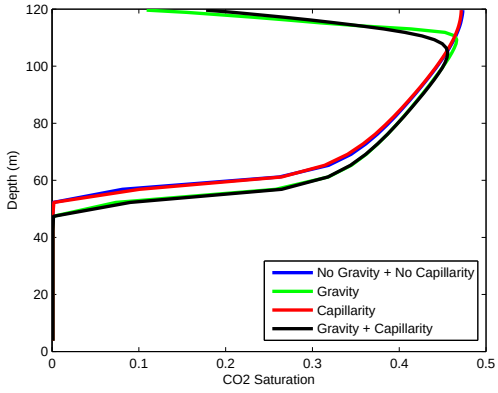

(c)

FIGURE 6. CO_2 saturation against the depth for the homogeneous domain consists of four layers at (a) $x = 3.7$m, (b) $x = 8.9$m, and (c) $x = 34.2$m.

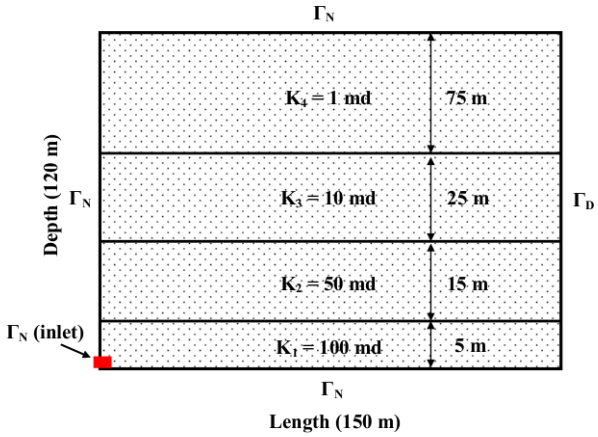

FIGURE 7. Permeability distributions of the layered porous medium: Example 2.

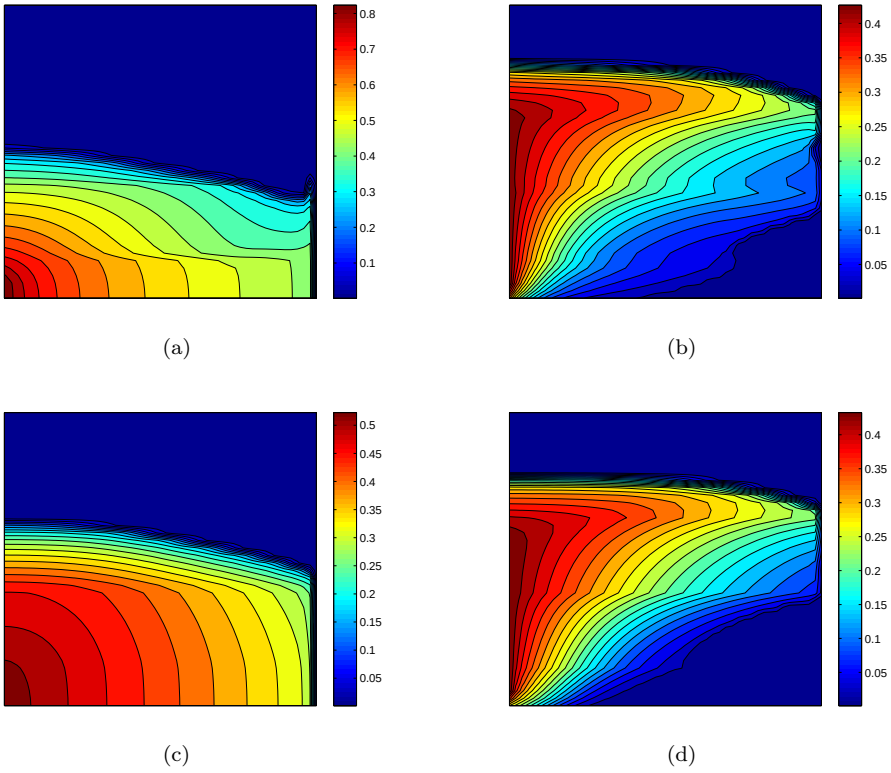

FIGURE 8. CO_2 saturation profiles in the layered domain after one year of injection for four different cases: (a) without the gravity and the capillarity, (b) the gravity effect only, (c) the capillarity effect only, and (d) with the gravity and the capillarity.

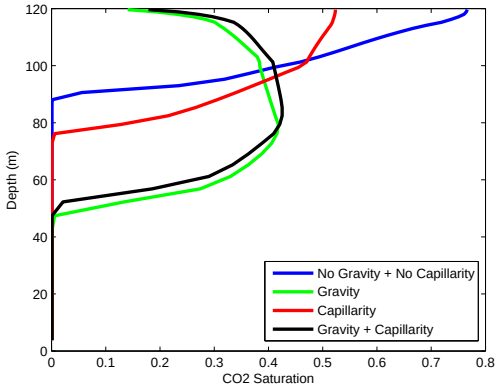

(a)

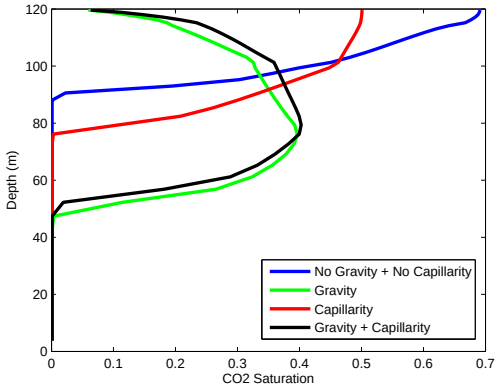

(b)

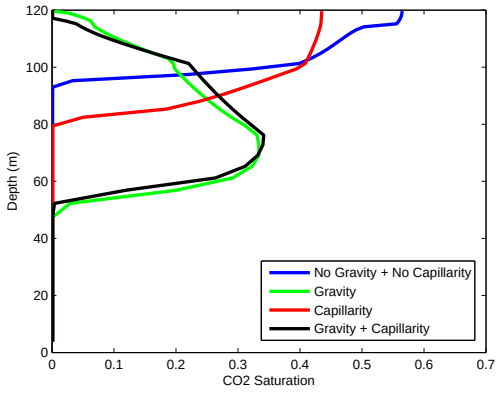

(c)

FIGURE 9. CO_2 saturation against the depth for the heterogeneous domain consists of four layers at (a) $x = 3.7$m, (b) $x = 8.9$m, and (c) $x = 34.2$m.

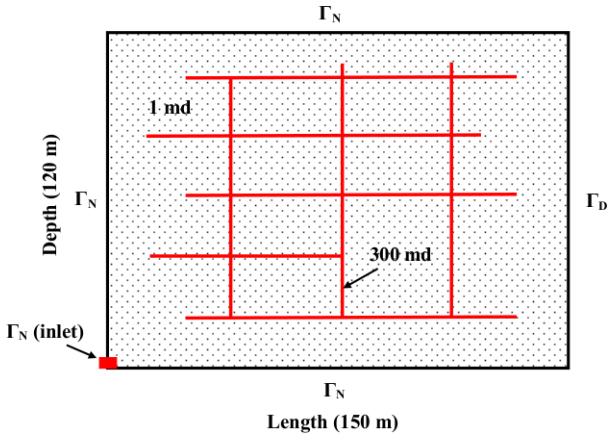

FIGURE 10. Permeability distributions of the fractured porous medium: Example 3.

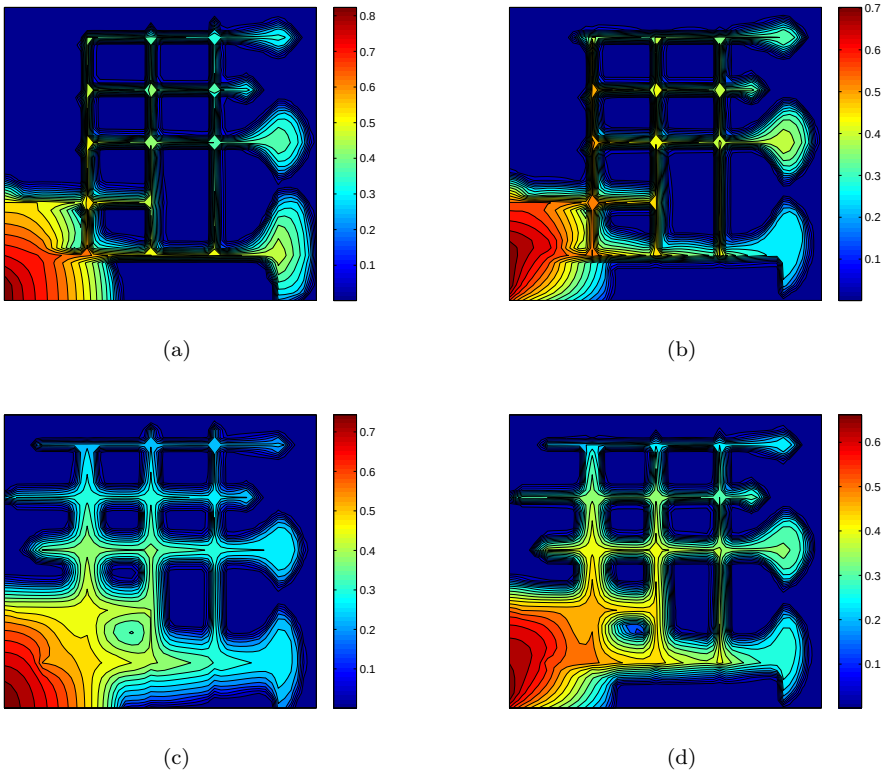

FIGURE 11. CO_2 saturation profiles in the fractured domain after one year of injection for four different cases: (a) without the gravity and the capillarity, (b) the gravity effect only, (c) the capillarity effect only, and (d) with the gravity and the capillarity.

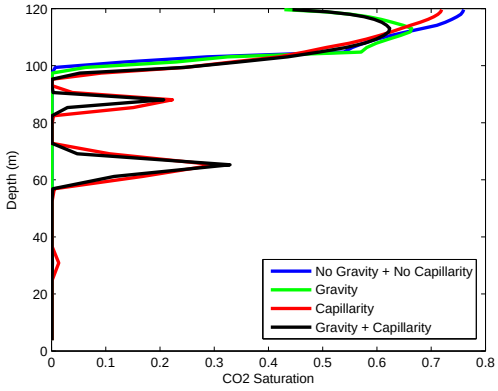

(a)

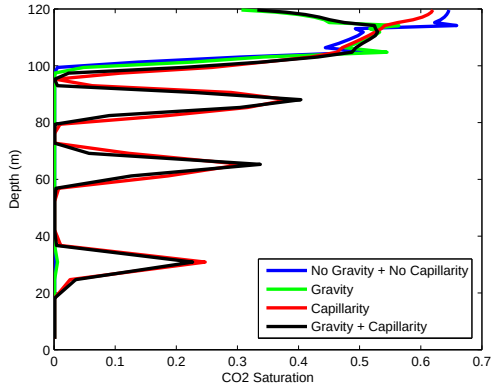

(b)

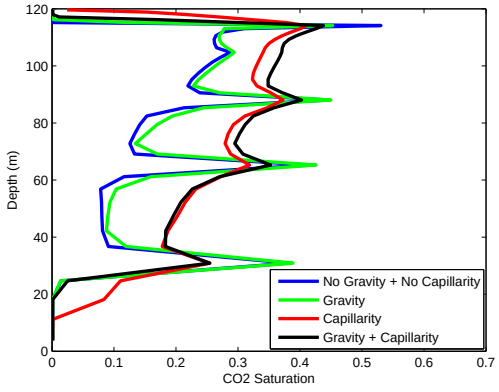

(c)

FIGURE 12. CO_2 saturation against the depth for the fractured domain at (a) $x = 3.7$m, (b) $x = 8.9$m, and (c) $x = 34.2$m.